NANO LETTERS

Letter

pubs.acs.org/NanoLett

Observation of Switchable Photoresponse of a Monolayer WSe_2–MoS_2 Lateral Heterostructure via Photocurrent Spectral Atomic Force Microscopic Imaging

Youngwoo Son,[†] Ming-Yang Li,[‡,§] Chia-Chin Cheng,[∥] Kung-Hwa Wei,[∥] Pingwei Liu,[†] Qing Hua Wang,[⊥] Lain-Jong Li,[‡] and Michael S. Strano*[,†]

[†]Department of Chemical Engineering, Massachusetts Institute of Technology, Cambridge, Massachusetts 02139, United States

[‡]Physics Science and Engineering Division, King Abdullah University of Science and Technology, Thuwal 23955-6900, Kingdom of Saudi Arabia

[§]Research Center for Applied Sciences, Academia Sinica, Taipei 10617, Taiwan

[∥]Department of Material Science and Engineering, National Chiao Tung University, Hsinchu 300, Taiwan

[⊥]Materials Science and Engineering, School for Engineering of Matter, Transport and Energy, Arizona State University, Tempe, Arizona 85287, United States

S *Supporting Information*

ABSTRACT: In the pursuit of two-dimensional (2D) materials beyond graphene, enormous advances have been made in exploring the exciting and useful properties of transition metal dichalcogenides (TMDCs), such as a permanent band gap in the visible range and the transition from indirect to direct band gap due to 2D quantum confinement, and their potential for a wide range of device applications. In particular, recent success in the synthesis of seamless monolayer lateral heterostructures of different TMDCs via chemical vapor deposition methods has provided an effective solution to producing an in-plane p–n junction, which is a critical component in electronic and optoelectronic device applications. However, spatial variation of the electronic and optoelectonic properties of the synthesized heterojunction crystals throughout the homogeneous as well as the lateral junction region and the charge carrier transport behavior at their nanoscale junctions with metals remain unaddressed. In this work, we use photocurrent spectral atomic force microscopy to image the current and photocurrent generated between a biased PtIr tip and a monolayer WSe_2–MoS_2 lateral heterostructure. Current measurements in the dark in both forward and reverse bias reveal an opposite characteristic diode behavior for WSe_2 and MoS_2, owing to the formation of a Schottky barrier of dissimilar properties. Notably, by changing the polarity and magnitude of the tip voltage applied, pixels that show the photoresponse of the heterostructure are observed to be selectively switched on and off, allowing for the realization of a hyper-resolution array of the switchable photodiode pixels. This experimental approach has significant implications toward the development of novel optoelectronic technologies for regioselective photodetection and imaging at nanoscale resolutions. Comparative 2D Fourier analysis of physical height and current images shows high spatial frequency variations in substrate/MoS_2 (or WSe_2) contact that exceed the frequencies imposed by the underlying substrates. These results should provide important insights in the design and understanding of electronic and optoelectronic devices based on quantum confined atomically thin 2D lateral heterostructures.

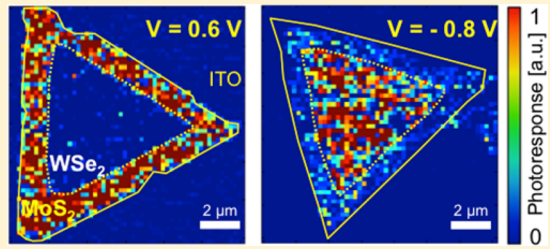

KEYWORDS: *Two-dimensional materials, MoS_2, WSe_2, transition metal dichalcogenides, heterostructure, photoresponsivity*

The significant interest and research effort devoted to discovering two-dimensional (2D) crystals beyond graphene have resulted in substantial progress in the fundamental understanding of transition metal dichalcogenides (TMDCs) with important implications for the design of future nanoelectronic components.[1,2] Many TMDCs possess unique electronic and optical properties including permanent band gaps as well as transitions from indirect to direct characteristic originating from 2D quantum confinement. These properties have motivated their exploration as active materials for a broad range of electronic[3−7] and optoelectronic[8−14] applications. Materials for such applications require the development of versatile junctions such as 2D/metal[15−17] or 2D/2D Schottky[18−20] and in particular p–n junctions.[21−23] Traditional doping methods such as dopant diffusion and ion-implantation used for conventional bulk semiconductors are not generally suitable for atomically thin 2D layers due to unavoidable crystal damage, so significant effort has been focused on achieving

Received: February 17, 2016
Revised: April 12, 2016
Published: April 27, 2016

DOI: 10.1021/acs.nanolett.6b00699
Nano Lett. 2016, 16, 3571−3577

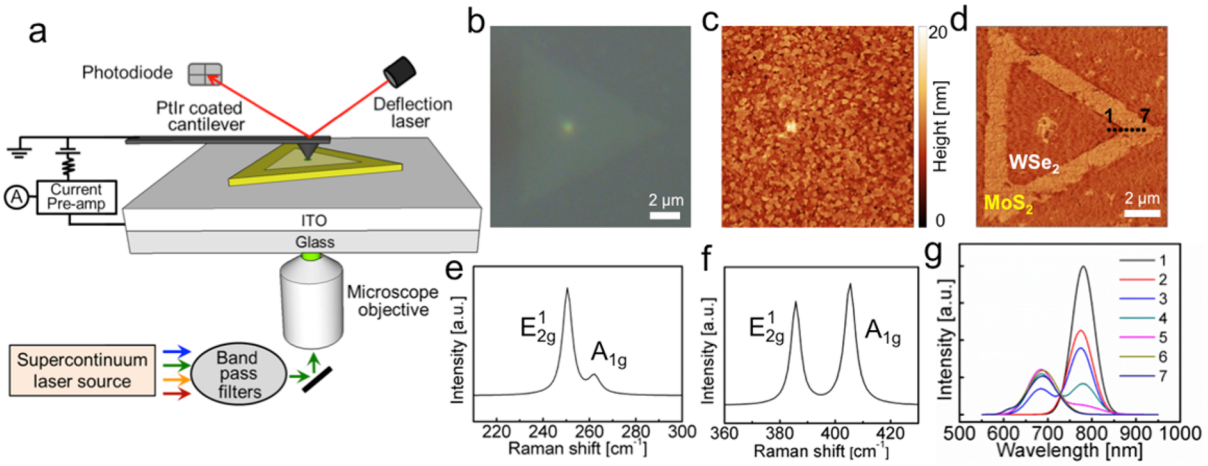

Figure 1. (a) Schematic illustration of the photoconductive spectral atomic force microscope (PCS-AFM) instrument and WSe_2−MoS_2 heterostructure crystal. (b−d) Optical microscope image, AFM topographic image, and lateral force microscopy (LFM) image of a WSe_2−MoS_2 heterostructure crystal on ITO/glass substrate. (e−g) Representative Raman spectra taken at each homogeneous crystal region of (e) WSe_2, (f) MoS_2, and from the locations along the dashed line marked in (d).

vertical van der Waals p−n heterostructures of dissimilar TMDCs of n- and p-types.[22,24,25] While the vertical heterostructure exhibits both characteristic rectifying behavior and photovoltaic response, the transfer process used to form a vertical p−n junction is insufficiently robust because it introduces unwanted trap states, lattice mismatch, and spatial inhomogeneity. Recently, a promising alternative route in the form of a monolayer in-plane p−n junction was developed via a two-step epitaxial growth of p-type WSe_2 and n-type MoS_2. By removing the laborious and unreliable transfer process of vertical heterojunctions and significantly improving the interface quality, the in-plane heterojunction shows tremendous promise for the realization of TMDC monolayer components in future nanoelectronics.[26] Although this seamless WSe_2−MoS_2 lateral heterojunction crystal showed clear rectifying behavior, photoresponse, and photovoltaic effects, many questions about the spatial dependence of nanoscale local electrical and optoelectronic properties, not only throughout the homogeneous crystals but at the lateral junction regions, remain unaddressed.

In this report, we answer these important questions using conductive and photocurrent spectral atomic force microscopy (C-AFM and PCS-AFM) measurements to obtain the spatially resolved transverse electrical properties of the monolayer WSe_2−MoS_2 lateral p−n heterostructures both in the dark and under laser illumination. We have previously reported that C- and PCS-AFM are versatile tools to conveniently and efficiently interrogate layer-dependent electronic and optoelectronic characteristics in a MoS_2 crystal containing regions of different thicknesses, enabling direct characterization and comparison of the different layer regions without the complexities associated with fabricating and testing of different individual field-effect transistor devices.[27] By performing current imaging using a PtIr-coated conductive tip on an ultrathin nanosheet that includes homogeneous crystals of WSe_2 and MoS_2 and a lateral junction region in between, we can form many thousands of WSe_2/MoS_2/the junction−metal contact points during imaging and directly compare their local properties at the same time under identical experimental conditions with the nanoscale spatial resolution. Therefore, in this work we study for the first time spatial dependence of electronic and optoelectronic characteristics of a monolayer WSe_2−MoS_2 lateral heterostructure via current imaging of the nanosheets that can fit within a single AFM image in both forward and reverse bias regimes using the C- and PCS-AFM. In addition, we show that by changing the polarity and magnitude of the applied voltage the photoresponse pixels in part of the heterostructure are selectively switched on and off, demonstrating a hyper-resolution switchable photodiode array.

Results and Discussion. *Carrier Transport in the Dark.* Previously, we have shown that extracting averaged current−voltage (I−V) characteristics from a series of C-AFM images with varying applied voltages is superior over taking I−V curves at fixed positions in that it generates not only more accurate and reliable I−V curves but additional information about spatial inhomogeneity in local charge distributions, local defects, sample edges, and local tip−sample interactions.[27] Thus, throughout this work we record the current through the C-AFM tip while imaging and varying the applied sample bias. Because the monolayer WSe_2−MoS_2 crystal is comprised of regions of homogeneous WSe_2, MoS_2, and the lateral junction in between that can fit within a single AFM image, we can directly compare electrical properties of regions obtained under identical experimental conditions.

In order to study carrier transport in the dark, a monolayer lateral WSe_2−MoS_2 heterostructure was synthesized on *c*-plane sapphire substrates by sequential chemical vapor deposition (CVD) of WSe_2 and MoS_2, followed by transfer onto a conductive indium tin oxide (ITO)-coated glass substrate.[26,28,29] The crystals were first identified by optical contrast and then their identity and thickness were verified using Raman and photoluminescence (PL) spectroscopy. The C-AFM and PCS-AFM measurements were conducted using PtIr-coated conductive probes in contact imaging mode. During the measurements, the conductive tip is held at ground while the bias voltage was applied to the ITO substrate as the other electrode. Throughout this paper, we refer to forward (reverse) bias when the ITO electrode is positively (negatively) biased relative to the grounded conductive tip. More details can be found in the Experimental Methods section in the Supporting Information.

The experimental setup for our C-AFM and PCS-AFM measurements is illustrated in Figure 1a. An optical image and the AFM topography of the transferred lateral heterostructure

DOI: 10.1021/acs.nanolett.6b00699
Nano Lett. 2016, 16, 3571−3577

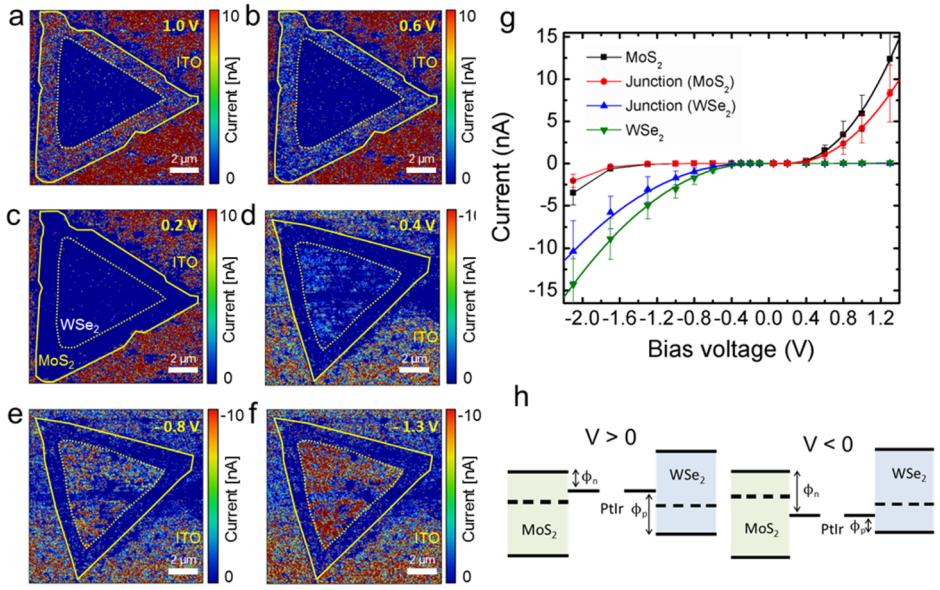

Figure 2. (a–f) Current maps generated by conductive AFM measurements in the dark under applied sample bias voltages of (a) 1.0, (b) 0.6, (c) 0.2, (d) −0.4, (e) −0.8, and (f) −1.3 V. (g) Averaged *I*–*V* data extracted from the homogeneous and lateral junction regions of WSe_2 and MoS_2. (h) A schematic band diagram of a WSe_2/MoS_2–PtIr metal tip junction under forward (left) and reverse (right) sample bias voltages.

are shown in Figure 1b,c, respectively, where the in-plane junction in the triangular nanosheet is difficult to identify. For better visualization, a lateral force microscopy (LFM) image of the nanosheet was taken (Figure 1d), which allows for the overall crystal shape and the lateral junction that distinguishes a region of WSe_2 from that of MoS_2 to be clearly seen. We identified the thickness of this crystal by its Raman spectrum, where the prominent peaks of WSe_2 at 250 and 260 cm^{-1} (Figure 1e), assigned to $E_{2g}{}^1$ and A_{1g} modes,[29] and the two signature Raman peaks of MoS_2 in Figure 1f, the $E_{2g}{}^1$ and A_{1g} peaks with the frequency difference (Δ) of 19.6 cm^{-1}, confirm that the flake is comprised of a monolayer WSe_2 crystal surrounded by a monolayer MoS_2 crystal.[30] The monolayer nature of the crystal is further confirmed by strong photoluminescence (PL) signals collected from the locations marked in Figure 1d, as shown in Figure 1g.

In order to study the spatial dependence of local *I*–*V* characteristics of the heterostructure at its nanoscale junction with the conductive metal tip, a sequence of images were obtained at varying values of the applied bias voltage, as shown in Figure 2a–c (forward bias) and Figure 2d–f (reverse bias) where the numbers on the top right side of each image indicate the sign and magnitude of the applied voltages (images for additional voltage values are presented in the Supporting Information). In contrast to the bare ITO surface showing high conductivity, the nanosheet introduces additional resistance against current flow, resulting in noticeable nonlinear behavior as a function of applied voltage. In the forward bias regime, the current increases noticeably in the MoS_2 region whereas there is almost no current increase detected in the WSe_2 region; the opposite trend is observed in the reverse bias regime. This response suggests the formation of an energy barrier at the nanoscale junction between the metal tip and the semiconducting 2D crystals in both forward and reverse bias regimes. We note that there is some small degree of spatial inhomogeneity that may result from variations in local barrier heights arising from impurities, defects, and fluctuations in tip–sample contact. However, the possibilities of tip degradation affecting the current measurements can be excluded, as we have shown in our previous report by stable force–distance curves obtained throughout the series of measurements.[27]

We then obtained *I*–*V* curves by averaging the current values from each voltage image at a particular region of the sample: the homogeneous MoS_2 crystal, the homogeneous WSe_2 crystal, and a junction region near the boundary of the two compositions. Since earlier scanning Kelvin probe microscopy (SKPM) measurements on the heterostructure revealed that the depletion width across the lateral junction is ∼320 nm,[26] current values for the junction were extracted from pixels that are within ∼120 nm of the boundary toward homogeneous crystals of MoS_2 and WSe_2. The junction boundary is determined from the lateral force image (Figure 1d) in which the borderline can be identified clearly due to the difference in force fields the metal tip experiences when scanning over the crystal regions of WSe_2 and MoS_2. Figure 2g shows the averaged *I*–*V* curves from the homogeneous WSe_2 and MoS_2 crystals, as well as both WSe_2 and MoS_2 sides of the junction in between them, where the error bars indicate the standard deviations from all the pixels within the current images at each given voltage. The green triangles, black squares, blue triangles, and red indicate data points acquired from each of the WSe_2, MoS_2, and lateral junction regions of WSe_2 and MoS_2, respectively, under identical experimental conditions. Because we average over many thousands of data points for each voltage, a reliable *I*–*V* curve can be obtained.

The *I*–*V* curves in Figure 2g show nearly insulating behavior at low bias voltages and abrupt nonlinear increases in current at high bias voltage in both the reverse and forward bias regimes. This is in good agreement with our prior finding that the nanojunction between atomically thin 2D layers and the metal tip gives rise to the characteristic rectifying carrier transport behavior due to the formation of the junction energy barrier, which is impacted by both barrier height and width.[27] This is well explained by Fowler–Nordheim (FN) tunneling model that is widely adopted as a model for describing charge carriers tunneling from the Fermi level of a metal to an adjacent

DOI: 10.1021/acs.nanolett.6b00699
Nano Lett. 2016, 16, 3571–3577

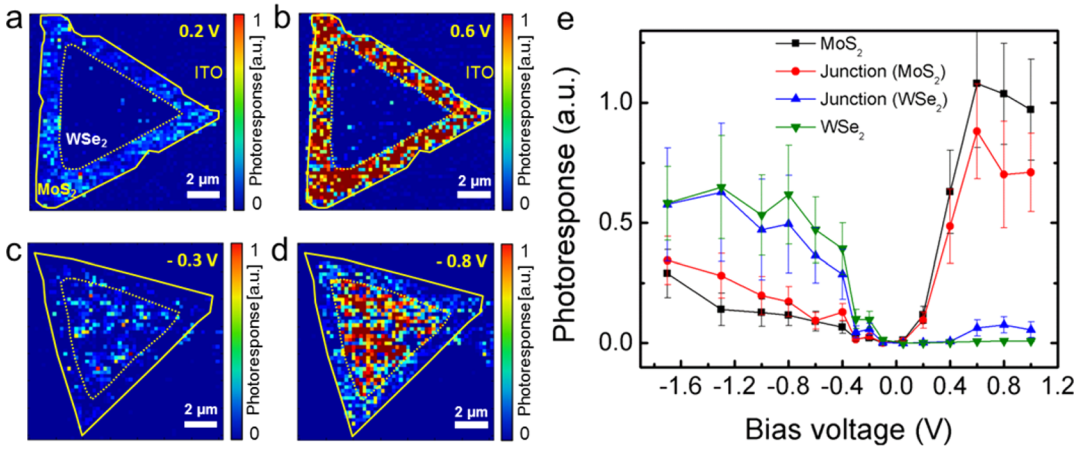

Figure 3. (a–d) Photoresponse maps at forward bias voltages of (a) 0.2 and (b) 0.6 V, and reverse bias voltages of (c) −0.3 V and (d) −0.8 V under illumination of λ = 550 nm. (e) Plot of photoresponse versus voltage with the error bars indicating standard deviations.

material through a junction barrier.[31] Even though charge carriers experience the resistance of an atomically thin layer of almost the same thickness (~0.7 nm), I–V curves obtained from WSe_2 and MoS_2 show an entirely different trend: the conductivity of WSe_2 increases exponentially as reverse bias voltage increases without noticeable current recorded in the forward range, whereas the opposite is the case for MoS_2. This corroborates the interpretation of the carrier transport mechanism proposed in our previous paper by expanding to new systems.

Schematic illustrations in Figure 2h show the band structures of the PtIr/WSe_2 and PtIr/MoS_2 systems under applied biases: forward bias ($V > 0$) is shown on the left and reverse bias ($V < 0$) is shown on the right. When the metal tip is brought into contact with a thin WSe_2 or MoS_2 crystal, the difference between the metal work function and the valence (conduction) band edge of WSe_2 (MoS_2), based on the Schottky–Mott theory,[32] causes a Schottky barrier to form at the interface. Because of the p-type nature of WSe_2, when it is in contact with the PtIr tip whose work function is ~5.4 eV,[33] the equilibrium Fermi level locates close to the valence band edge.[34] In the case of n-type MoS_2, partial Fermi level pinning positions the equilibrium energy near the conduction band edge.[35]

Both the electron and the hole currents beyond a certain threshold voltage include two contributions: the tunneling events through the Schottky barrier and thermionic emission current over the top of the energy barrier. At the junction between WSe_2 and the PtIr metal tip, the Schottky barrier height for hole injection into the valence band of WSe_2 (ϕ_p) is lower than that for electron injection into the conduction band (ϕ_n). In the reverse bias regime, the barrier height and width is reduced with higher applied voltage, resulting in an enhanced probability of field emission tunneling through the barrier. When the forward bias voltage is applied, the likelihood of hole tunneling events is suppressed to its lowest saturation and the thermionic emission contribution becomes increasingly smaller with voltage due to the raised Schottky barrier height, ϕ_p. In contrast, when the interface between MoS_2 and the metal tip is considered (here, ϕ_n is smaller than ϕ_p), the barrier width becomes smaller as higher voltage is imposed, enhancing the tunneling contribution dramatically in the forward bias regime, while more negative voltage constrains the tunneling to its lowest and thermionic emission to further reduced level due to thickened junction barrier and an eventual increase of ϕ_n.

This stark difference of electrical properties between the two single-layered component crystals of the lateral heterostructure highlights a critical role of the nature of the junction barrier on carrier transport behavior through the nanoscale metal-atomically thin 2D crystal interface. In addition, it is notable that the junction regions of both WSe_2 and MoS_2 exhibit lower conductivity than corresponding homogeneous regions throughout the whole voltage range of our measurements. We attribute the origin of this observation to the change in the energy of the conduction and valence band edges over the depletion width of the lateral p–n junction. On the WSe_2 side of the depletion region, the energy of the valence band edge gradually decreases, rendering ϕ_p larger compared to its homogeneous counterpart when in contact with the metal tip. The fact that the subtle change in the electronic properties of the lateral junction region of the sample is detected highlights the sensitivity of the measurements offered by the PCS-AFM instrument, which could be especially beneficial to answer many interesting questions about nanomaterials with complex heterojunctions. Similarly, for the MoS_2 side of the region, because the conduction band energy rises as it comes closer to homogeneous WSe_2, ϕ_n becomes higher hindering electron injection to this region to some extent. This finding of differing junction behavior further corroborates the sensitivity of carrier transport at the nanoscale metal–2D layer interface on the junction barrier characteristics.

In order to extract the barrier heights for electron injection to the conduction band of MoS_2 ($\phi_{n,MoS2}$) and hole injection to the valence band of WSe_2 ($\phi_{p,WSe2}$), following our previous publication,[27] we use the FN tunneling theory, which is widely adopted as a model for describing electrons tunneling from the Fermi level of a metal to an adjacent material through a junction barrier with the current I described by[31]

$$I(V) = \frac{A_e q^3 m V^2}{8\pi h \phi_B d^2 m^*} \exp\left[\frac{-8\pi\sqrt{2m^*}\,\phi_B^{3/2} d}{3hqV}\right] \quad (1)$$

where A_e denotes the effective contact area, q is the electronic charge, V is the applied bias voltage, h is Planck's constant, ϕ_B is the barrier height, d is the distance between the electrodes, and m^* is the effective mass. The experimental I–V data in Figure 2g are fit to the FN tunneling model in eq 1 (solid black, red, green, and blue lines for MoS_2, MoS_2 junction, WSe_2, and WSe_2 junction, correspondingly). We see that the FN model agrees

DOI: 10.1021/acs.nanolett.6b00699
Nano Lett. 2016, 16, 3571–3577

well with the data and the effective barrier height can be extracted from the fitting to the model to be 0.58, 0.60, 0.62, and 0.65 eV, for $\phi_{n,MoS2}$, $\phi_{n,MoS2}$,junc, $\phi_{p,WSe2}$, and $\phi_{p,WSe2}$,junc, respectively. The extracted $\phi_{n,MoS2}$ in the present work is close to but slightly lower than the value estimated for a micromechanically exfoliated monolayer MoS_2 using the same experimental setup, 0.61 eV.[27] This can be attributed to the fact that the work function of the synthesized and mechanically exfoliated MoS_2 crystals may somewhat differ from each other, and dissimilar ITO substrates could lead to different interactions with the sitting 2D crystals that consequently give rise to changes in the junction properties.

Voltage Selectable Photoresponse. Because this monolayer in-plane p−n heterostructure possesses an enormous potential to play a major role as an active component over a wide variety of future nanoscale optoelectronic devices, we also explore its photoresponse using the PCS-AFM measurements to answer important questions about spatial variation of its local optoelectronic properties. We use the same heterostructure nanosheet that was featured in Figure 2 for these optoelectronic measurements in order to directly compare the results to the dark current behavior. The analysis conducted for dark current can be expanded to interpret strong dependence of photocurrent on the applied voltage. Figure 3a−d shows spatially resolved photoresponse maps of the sample, in both forward (a,b) and reverse voltage regimes (c,d). The bias voltages are varied while the illumination is maintained at λ = 550 nm (see the Supporting Information for additional photoresponse images at different voltages as well as current images in dark and light). The photoresponse is defined as the difference between photocurrent (I_L) and dark current (I_D) normalized by illumination power

$$\text{photoresponse} = \frac{\frac{I_L - I_D}{q}}{\frac{P_{inc}}{h\nu}} \quad (2)$$

where q is electronic charge, P_{inc} is the incident power, and $h\nu$ is the photon energy. These photoresponse maps are generated by subtracting a photocurrent map under illumination from a dark current map, and normalized by the incident laser power at a selected wavelength. It is important to note that the wavelength dependence of photoresponse of MoS_2 detected using this instrument in our prior report[27] shows that the enhanced current under illumination is predominantly due to interband photoexcitation in a 2D material being interrogated rather than absorption or heating effects in the metal tip.

In the photoresponse maps (Figure 3), a small level of spatial irregularities is observed due to local variability of electrical properties of the junction with the metal tip. Pixels within the boundaries of an each homogeneous crystal region in general show reasonably constant photoresponse intensities over the entire sample area, demonstrating stability and reliability of our measurements. Under small magnitude applied sample voltages (Figure 3a,c), both WSe_2 and MoS_2 generate a very small degree photoresponse. But interestingly, when we apply a larger magnitude voltage in the forward bias regime, the pixels in the MoS_2 region clearly turn on while those in the WSe_2 region remain dark (Figure 3b). Moreover, by applying the opposite polarity and large magnitude bias voltage, as depicted in Figure 3d, the MoS_2 pixels can be switched off while turning the WSe_2 pixels on. The degree of this photoresponse switching, a relative photoresponse of one region to another, can effectively be modulated by the magnitude of the applied sample voltage (see Supporting Information for photoresponse maps under varying voltages). That is, by utilizing this experimental approach, a nanoscale high-resolution array of switchable photodiode pixels can be realized.

The photoresponse as a function of voltage was plotted by taking the average photoresponse over each of the homogeneous and junction regions, as shown in Figure 3e, where error bars indicate the standard deviation. We note that the photoresponse in forward and reverse bias regimes exhibits obvious barrier asymmetry for both WSe_2 and MoS_2 and shows a nonlinear increasing trend in all regions as the bias voltage is raised. In our previous report, we showed that major factors influencing the photoresponse detected by the PCS-AFM system are light absorption, photoexcited carrier separation, and carrier collection efficiencies.[27] Because we explore the heterostructure crystal of uniform thickness (monolayer), the pixels in the same region should have almost the same absorption efficiency, given the absorption coefficients are similar at 550 nm illumination,[36] thereby making the light absorption factor negligible in the interpretation of the bias-dependent photoresponse trend of each region, as compared to the other two contributions. The importance the carrier collection efficiency contribution (effective transport of photoexcited carriers through the nanoscale metal−2D layer junction to be collected by the metal tip) to the overall photoresponse becomes evident when comparing photoresponse values of WSe_2 and MoS_2 acquired with high bias voltages applied in the reverse and forward range, respectively. Under these high drive bias voltages, there is enough external driving force to effectively separate photoexcited charge carriers such that the effectiveness of exciton dissociation becomes insignificant, allowing for the carrier collection events to dominate the process. We observe that the photoresponse of WSe_2 under this condition in the reverse range is lower than that of MoS_2 in the forward regime, which is in accordance with the dark current trend shown in Figure 2g in which absolute current values are smaller in WSe_2 than MoS_2 for equal absolute sample bias voltages. The fact that WSe_2 (MoS_2) generates a very low level of the response throughout the forward (reverse) regime can also be ascribed to the reduced carrier collection efficiency because of the increased effective junction barrier. Although it may be possible that small contributions to this difference may originate from different absorption coefficients of the two for a chosen laser wavelength,[37] the overall trend is mostly determined by the transport characteristic.

The photoresponse in both WSe_2 and MoS_2 rises sharply in a nearly linear fashion in the reverse and forward regime, respectively, as the absolute sample voltage is raised until around 0.8 V, owing to the increasingly improved carrier transport and a larger amount of energy available for carrier separation, and becomes relatively flat without showing notable increase afterward. It can be because the 0.8 V of drive voltage provides enough energy to separate and collect most of the photoexcited charge carriers. In forward (reverse) bias for WSe_2 (MoS_2), however, photoexcited carriers face a barrier at the junction with the metal tip that needs to be thermally overcome or tunneled through to be detected, and the barrier that remains in the voltage range of our experiment can lead to the observed forward−reverse asymmetry. In the junction region of both WSe_2 and MoS_2, the response shows a dissimilar behavior under forward and reverse bias voltages: lower (higher) in the reverse regime but higher (lower) under the forward bias for

DOI: 10.1021/acs.nanolett.6b00699
Nano Lett. 2016, 16, 3571−3577

WSe_2 (MoS_2) in comparison with its homogeneous counterpart. This result suggests that the overall photocurrent is almost entirely determined by the carrier transport process, which is mainly influenced by change in the band edge energy in the depletion region in one bias voltage regime, whereas the built-in electric field enhancement at the lateral p−n junction can give rise to an additional contribution to photocurrent when the bias polarity is flipped. This understanding of photocurrent generation from a WSe_2−MoS_2 lateral heterostructure will provide useful insight into developing a high-resolution array of nanoscale photodetector units with an optimized photoresponse ratio between component pixels by the selection of the specific polarity and magnitude of voltage to achieve for targeted purposes, which can be further tuned by modulating illumination laser wavelengths as well as the layer number of component materials.

In our previous report,[27] we explained the sublinear illumination power dependence of photocurrent by a kinetic model that accounts for the rapid exciton−exciton annihilation (EEA)[38] in atomically thin MoS_2 crystals (see Supporting Information for the details). In the model, the exciton density is expressed with loss terms by the EEA and exciton dissociation, and a generation term that is dependent on the laser power and the layer thickness. Because residence time of the metal tip on each pixel while scanning is on the order of $\sim 10^{-3}$ s, which is substantially longer than an effective lifetime for excitons in a single layer MoS_2, the system is considered to have reached the steady state and the EEA rate constant (k_1) and the free carrier generation rate (dissociation of exciton, k_2) for a monolayer MoS_2 are extracted as k_1 (MoS_2) = 4.3×10^{-2} cm^2 s^{-1} and k_2 (MoS_2) = 3.3×10^{-1} s^{-1}. By adopting these constants and assuming that the ratio of k_1 to k_2 for WSe_2 is the same as for MoS_2 in consideration of the similar exciton binding energy,[39] the ratio of the averaged photocurrent in MoS_2 to that in WSe_2 recorded under a 0.6 V magnitude of voltage at 550 nm, which are the same experimental conditions as the prior report, yields k_1 (WSe_2) = 9.5×10^{-3} cm^2 s^{-1} and k_2 (WSe_2) = 7.3×10^{-2} s^{-1}. Here, the extinction coefficient at 550 nm is set to be $\varepsilon_{MoS_2}/\varepsilon_{WSe_2} \sim 1.2$.[36]

Spatial Analysis. We conducted spatial analysis of the AFM topography and current images in order to clarify the role of the ITO substrate on current measurements. Figure 4 shows topographic (a,c,e) and current (b,d,f) images simultaneously obtained with an applied sample bias of 0.7 V. The effect of the underlying substrate was investigated in detail by further comparing regions of the substrate with and without a MoS_2 crystal sitting on top, as indicated in Figure 4 panels a and b. The 2D fast Fourier transforms (FFTs) were performed on the bare substrate and substrate+MoS_2 regions of the topographic (Figure 4g,i) and current images (Figure 4h,j). It is observed that the intensity of both of the FFTs of the topography is mostly concentrated in the center region but that of the substrate-only region in the current image exhibits a concentric but dispersed feature; also, a more dispersed and an increased intensity along the vertical direction is observed in the substrate + MoS_2 region. These results reveal that there exists some degree of spatial correlation between the topography and current of the bare substrate but the correlation weakens with the introduction of an atomically thin nanosheet. We attribute these findings to imperfect contact between the nanosheets, the substrate, and the metal tip, which can be aggravated because of the fast tip movement. More fluctuations observed in the substrate + MoS_2 region of the current image can originate from the nature of the measurements: the charge carriers have to physically flow from the substrate through the nanosheets to the metal tip, which makes the current more sensitive to irregularities or small changes in the contact qualities between the components in contact mode imaging.

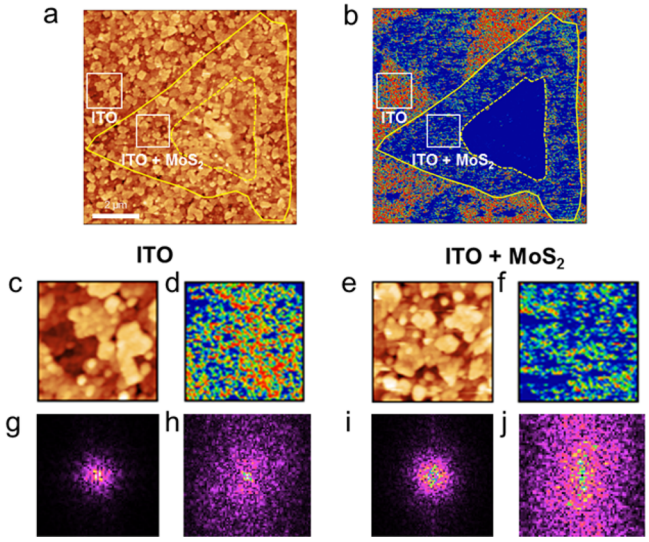

Figure 4. (a) Topographic height AFM image of a WSe_2−MoS_2 nanosheet. (b) A simultaneously obtained current image at sample bias of 0.7 V. The ITO-only region is enlarged in (c,d) and the ITO + MoS_2 region in (e,f). (g−j) The 2D FFTs of the images in (c−f).

Conclusions. In conclusion, we utilized the C- and PCS-AFM measurements to thoroughly investigate current transport mechanisms and photoresponse of a monolayer lateral WSe_2−MoS_2 heterostructure at its nanoscale junctions with the conductive metal tip. WSe_2 and MoS_2 show the opposite trend due to the different junction barrier properties while relatively lower conductivity is recorded in the lateral junction region because of the energy change in the valence and conduction band edges. A prominent voltage-dependent photoresponse was observed in both WSe_2 and MoS_2 in the reverse and forward sample bias regime, respectively. Notably, by modulating the polarity and magnitude of the applied voltage, the photoresponse pixels in a portion of the heterostructure crystal was observed to be selectively switched on and off, allowing for a high-resolution array of the switchable photodiode pixels to be demonstrated. These results shed light on the realization of future optoelectronic nanoscale devices for regioselective photodetection and imaging as well as nanoelectronic devices based on various types of monolayer lateral heterostructures in general.

■ ASSOCIATED CONTENT

Supporting Information

Experimental methods, discussion on the sample/ITO interface, discussion on the possibility of piezoelectricity contributing to photoresponse, discussion on the possibility of photodoping contributing to photoresponse, additional conductive AFM (C-AFM) images, additional photoresponse map of WSe_2−MoS_2 nanosheet under illumination of λ = 550 nm, additional conductive AFM (C-AFM) images under illumination, a kinetic model including the effect of the rapid exciton−exciton annihilation (EEA) in an atomically thin crystal. Figures S1−S3. The Supporting Information is available free of charge

DOI: 10.1021/acs.nanolett.6b00699
Nano Lett. 2016, 16, 3571−3577

on the ACS Publications website at DOI: 10.1021/acs.nanolett.6b00699.

(PDF)

AUTHOR INFORMATION

Corresponding Author

*E-mail: strano@mit.edu.

Notes

The authors declare no competing financial interest.

ACKNOWLEDGMENTS

M.S. Strano acknowledges a grant from Eni S.p.A. in the frame of the eni-MIT Solar Frontiers Center for support of the SPICIER instrument development. Also, this work was supported by the AFOSR FATE MURI, Grant No. FA9550-15-1-0514. Development of software algorithms for SPICIER were was also supported in part by the U.S. Army Research Laboratory and the U.S. Army Research Office through the Institute for US Soldier Nanotechnologies, under contract number W911NF-13-D-0001. Y. Son is grateful for partial financial support from a Samsung Scholarship. L.J. Li acknowledges the support from King Abdullah University of Science and Technology, Ministry of Science and Technology Taiwan, and Taiwan Consortium of Emergent Crystalline Materials, and AOARD-134137 USA.

REFERENCES

(1) Novoselov, K. S.; Jiang, D.; Schedin, F.; Booth, T. J.; Khotkevich, V. V.; Morozov, S. V.; Geim, A. K. *Proc. Natl. Acad. Sci. U. S. A.* **2005**, *102* (30), 10451−10453.

(2) Wang, Q. H.; Kalantar-Zadeh, K.; Kis, A.; Coleman, J. N.; Strano, M. S. *Nat. Nanotechnol.* **2012**, *7* (11), 699−712.

(3) Cui, Y.; Xin, R.; Yu, Z.; Pan, Y.; Ong, Z.-Y.; Wei, X.; Wang, J.; Nan, H.; Ni, Z.; Wu, Y.; Chen, T.; Shi, Y.; Wang, B.; Zhang, G.; Zhang, Y.-W.; Wang, X. *Adv. Mater.* **2015**, *27* (35), 5230−5234.

(4) Larentis, S.; Fallahazad, B.; Tutuc, E. *Appl. Phys. Lett.* **2012**, *101* (22), 223104.

(5) Radisavljevic, B.; Whitwick, M. B.; Kis, A. *ACS Nano* **2011**, *5* (12), 9934−9938.

(6) Wang, H.; Yu, L.; Lee, Y.-H.; Shi, Y.; Hsu, A.; Chin, M. L.; Li, L.-J.; Dubey, M.; Kong, J.; Palacios, T. *Nano Lett.* **2012**, *12* (9), 4674−4680.

(7) Tosun, M.; Chuang, S.; Fang, H.; Sachid, A. B.; Hettick, M.; Lin, Y.; Zeng, Y.; Javey, A. *ACS Nano* **2014**, *8* (5), 4948−4953.

(8) Abderrahmane, A.; Ko, P. J.; Thu, T. V.; Ishizawa, S.; Takamura, T.; Sandhu, A. *Nanotechnology* **2014**, *25* (36), 365202.

(9) Zhang, W.; Chiu, M.-H.; Chen, C.-H.; Chen, W.; Li, L.-J.; Wee, A. T. S. *ACS Nano* **2014**, *8* (8), 8653−8661.

(10) Choi, W.; Cho, M. Y.; Konar, A.; Lee, J. H.; Cha, G.-B.; Hong, S. C.; Kim, S.; Kim, J.; Jena, D.; Joo, J.; Kim, S. *Adv. Mater.* **2012**, *24* (43), 5832−5836.

(11) Lee, H. S.; Min, S.-W.; Chang, Y.-G.; Park, M. K.; Nam, T.; Kim, H.; Kim, J. H.; Ryu, S.; Im, S. *Nano Lett.* **2012**, *12* (7), 3695−3700.

(12) Lopez-Sanchez, O.; Lembke, D.; Kayci, M.; Radenovic, A.; Kis, A. *Nat. Nanotechnol.* **2013**, *8* (7), 497−501.

(13) Yin, Z.; Li, H.; Li, H.; Jiang, L.; Shi, Y.; Sun, Y.; Lu, G.; Zhang, Q.; Chen, X.; Zhang, H. *ACS Nano* **2012**, *6* (1), 74−80.

(14) Sundaram, R. S.; Engel, M.; Lombardo, A.; Krupke, R.; Ferrari, A. C.; Avouris, P.; Steiner, M. *Nano Lett.* **2013**, *13* (4), 1416−1421.

(15) Cakir, D.; Sevik, C.; Peeters, F. M. *J. Mater. Chem. C* **2014**, *2* (46), 9842−9849.

(16) Das, S.; Chen, H.-Y.; Penumatcha, A. V.; Appenzeller, J. *Nano Lett.* **2013**, *13* (1), 100−105.

(17) Walia, S.; Balendhran, S.; Wang, Y.; Ab Kadir, R.; Sabirin Zoolfakar, A.; Atkin, P.; Zhen Ou, J.; Sriram, S.; Kalantar-zadeh, K.; Bhaskaran, M. *Appl. Phys. Lett.* **2013**, *103* (23), 232105.

(18) Sata, Y.; Moriya, R.; Morikawa, S.; Yabuki, N.; Masubuchi, S.; Machida, T. *Appl. Phys. Lett.* **2015**, *107* (2), 023109.

(19) Shih, C.-J.; Wang, Q. H.; Son, Y.; Jin, Z.; Blankschtein, D.; Strano, M. S. *ACS Nano* **2014**, *8* (6), 5790−5798.

(20) Tian, H.; Tan, Z.; Wu, C.; Wang, X.; Mohammad, M. A.; Xie, D.; Yang, Y.; Wang, J.; Li, L.-J.; Xu, J.; Ren, T.-L. *Sci. Rep.* **2014**, *4*, 5951.

(21) Ross, J. S.; Klement, P.; Jones, A. M.; Ghimire, N. J.; Yan, J.; Mandrus, D. G.; Taniguchi, T.; Watanabe, K.; Kitamura, K.; Yao, W.; Cobden, D. H.; Xu, X. *Nat. Nanotechnol.* **2014**, *9* (4), 268−272.

(22) Huang, L.; Huo, N.; Li, Y.; Chen, H.; Yang, J.; Wei, Z.; Li, J.; Li, S.-S. *J. Phys. Chem. Lett.* **2015**, *6* (13), 2483−2488.

(23) Zhang, Y. J.; Ye, J. T.; Yomogida, Y.; Takenobu, T.; Iwasa, Y. *Nano Lett.* **2013**, *13* (7), 3023−3028.

(24) Lee, C.-H.; Lee, G.-H.; van der Zande, A. M.; Chen, W.; Li, Y.; Han, M.; Cui, X.; Arefe, G.; Nuckolls, C.; Heinz, T. F.; Guo, J.; Hone, J.; Kim, P. *Nat. Nanotechnol.* **2014**, *9* (9), 676−681.

(25) Deng, Y.; Luo, Z.; Conrad, N. J.; Liu, H.; Gong, Y.; Najmaei, S.; Ajayan, P. M.; Lou, J.; Xu, X.; Ye, P. D. *ACS Nano* **2014**, *8* (8), 8292−8299.

(26) Li, M.-Y.; Shi, Y.; Cheng, C.-C.; Lu, L.-S.; Lin, Y.-C.; Tang, H.-L.; Tsai, M.-L.; Chu, C.-W.; Wei, K.-H.; He, J.-H.; Chang, W.-H.; Suenaga, K.; Li, L.-J. *Science* **2015**, *349* (6247), 524−528.

(27) Son, Y.; Wang, Q. H.; Paulson, J. A.; Shih, C.-J.; Rajan, A. G.; Tvrdy, K.; Kim, S.; Alfeeli, B.; Braatz, R. D.; Strano, M. S. *ACS Nano* **2015**, *9* (3), 2843−2855.

(28) Chiu, M.-H.; Zhang, C.; Shiu, H.-W.; Chuu, C.-P.; Chen, C.-H.; Chang, C.-Y. S.; Chen, C.-H.; Chou, M.-Y.; Shih, C.-K.; Li, L.-J. *Nat. Commun.* **2015**, *6*, 7666.

(29) Huang, J.-K.; Pu, J.; Hsu, C.-L.; Chiu, M.-H.; Juang, Z.-Y.; Chang, Y.-H.; Chang, W.-H.; Iwasa, Y.; Takenobu, T.; Li, L.-J. *ACS Nano* **2014**, *8* (1), 923−930.

(30) Lee, C.; Yan, H.; Brus, L. E.; Heinz, T. F.; Hone, J.; Ryu, S. *ACS Nano* **2010**, *4* (5), 2695−2700.

(31) Fowler, R. H.; Nordheim, L. *Proc. R. Soc. London, Ser. A* **1928**, *119* (781), 173−181.

(32) Rhoderick, E. H. *IEE Proc., Part I: Solid-State Electron Devices* **1982**, *129* (1), 1.

(33) Klaua, M.; Ullmann, D.; Barthel, J.; Wulfhekel, W.; Kirschner, J.; Urban, R.; Monchesky, T. L.; Enders, A.; Cochran, J. F.; Heinrich, B. *Phys. Rev. B: Condens. Matter Mater. Phys.* **2001**, *64* (13), 134411.

(34) Lee, I.; Rathi, S.; Li, L.; Lim, D.; Atif Khan, M.; Kannan, E. S.; Kim, G. H. *Nanotechnology* **2015**, *26* (45), 455203.

(35) Gong, C.; Colombo, L.; Wallace, R. M.; Cho, K. *Nano Lett.* **2014**, *14* (4), 1714−1720.

(36) Liu, H.-L.; Shen, C.-C.; Su, S.-H.; Hsu, C.-L.; Li, M.-Y.; Li, L.-J. *Appl. Phys. Lett.* **2014**, *105* (20), 201905.

(37) Flöry, N.; Jain, A.; Bharadwaj, P.; Parzefall, M.; Taniguchi, T.; Watanabe, K.; Novotny, L. *Appl. Phys. Lett.* **2015**, *107* (12), 123106.

(38) Sun, D.; Rao, Y.; Reider, G. A.; Chen, G.; You, Y.; Brézin, L.; Harutyunyan, A. R.; Heinz, T. F. *Nano Lett.* **2014**, *14* (10), 5625−5629.

(39) Ramasubramaniam, A. *Phys. Rev. B: Condens. Matter Mater. Phys.* **2012**, *86* (11), 115409.

DOI: 10.1021/acs.nanolett.6b00699
Nano Lett. 2016, 16, 3571−3577